Medical & Biological Engineering & Computing
https://doi.org/10.1007/s11517-018-1880-6

ORIGINAL ARTICLE

An automatic multi-class coronary atherosclerosis plaque detection and classification framework

Fengjun Zhao[1] · Bin Wu[1] · Fei Chen[2] · Xin Cao[1] · Huangjian Yi[1] · Yuqing Hou[1] · Xiaowei He[1] · Jimin Liang[2]

Received: 18 January 2018 / Accepted: 24 July 2018

Abstract
Detection of different classes of atherosclerotic plaques is important for early intervention of coronary artery diseases. However, previous methods focused either on the detection of a specific class of coronary plaques or on the distinction between plaques and normal arteries, neglecting the classification of different classes of plaques. Therefore, we proposed an automatic multi-class coronary atherosclerosis plaque detection and classification framework. Firstly, we retrieved the transverse cross sections along centerlines from the computed tomography angiography. Secondly, we extracted the region of interests based on coarse segmentation. Thirdly, we extracted a random radius symmetry (RRS) feature vector, which incorporates multiple descriptions into a random strategy and greatly augments the training data. Finally, we fed the RRS feature vector into the multi-class coronary plaque classifier. In experiments, we compared our proposed framework with other methods on the cross sections of Rotterdam Coronary Datasets, including 729 non-calcified plaques, 511 calcified plaques, and 546 mixed plaques. Our RRS with support vector machine outperforms the intensity feature vector and the random forest classifier, with the average precision of 92.6 ± 1.9% and average recall of 94.3 ± 2.1%. The proposed framework provides a computer-aided diagnostic method for multi-class plaque detection and classification.

Keywords Coronary atherosclerosis plaque · Detection · Classification · Computed tomography angiography

1 Introduction

Coronary artery disease (CAD) is the leading cause of death worldwide, including myocardial infarction and ischemic cardiomyopathy [8, 21]. CAD is closely related to coronary stenosis due to the burden of atherosclerotic plaques [9, 15]. Specifically, mixed atherosclerotic plaques take more responsibility for major cardiac adverse events compared with calcified and non-calcified plaques [1, 10]. Thus, detection and analysis of multi-class atherosclerotic plaques are of great importance for early prevention and intervention of CAD.

✉ Xiaowei He
hexw@nwu.edu.cn

✉ Jimin Liang
jimleung@mail.xidian.edu.cn

[1] School of Information Sciences and Technology, Northwest University, Xi'an 710069, Shaanxi, China

[2] Engineering Research Center of Molecular and Neuro Imaging of Ministry of Education, School of Life Science and Technology, Xidian University, Xi'an 710071, Shaanxi, China

Conventionally, invasive coronary angiography (ICA) is the gold standard imaging technique for the diagnosis of coronary plaques [4, 11]. However, the coronary arteries locating at different depths are visually overlapped with each other in two dimensional (2D) image, which increases the requirement of surgeons' experience. Computed tomography angiography (CTA) has gained popularity due to the advantages of non-invasive, three-dimensional (3D), and high-resolution imaging [22]. Nevertheless, the intensities of different classes of plaques (such as calcified plaques, non-calcified plaques, and mixed plaques) in CTA images vary widely. Moreover, motion artifacts caused by heartbeats and respiration deteriorate the quality of CTA images. Therefore, it remains a challenging task to accurately detect all classes of coronary atherosclerosis plaques.

1.1 State-of-the-art methods

Most of the previous automatic coronary plaque detection methods are intuitively devised with handcrafted rules. Toumoulin et al. picked out the area with higher intensity confined between the inner and outer coronary artery

Published online: 07 August 2018

boundaries as calcified plaques [26]. Wesarg et al. detected calcified plaques by combining the lumen radius with lumen intensity feature, based on the observation that the lumen of plaque artery was narrower compared with that of normal artery [29]. Similarly, Wang and Liatsis localized the calcified stenosis by assuming that normal arteries had circle-like cross sections, while cross sections of calcified stenosis deviated from being circular [28]. On the other hand, it has been demonstrated that high-resolution CTA imaging enables characterizing different components of coronary atherosclerosis plaques including necrotic cores, dense calcium, fibrotic, and fibro-fatty tissues [6]. Therefore, Rinck et al. proposed to detect non-calcified plaques by analyzing the discrepant areas between coronary artery lumens and walls based on CTA imaging [20]. Renard et al. decomposed the detection of non-calcified coronary plaques into three components: coronary artery centerline extraction, vessel lumen and wall segmentation, and plaque detection based on cross-section areas of lumen and wall [19]. Moreover, dual-energy CT imaging with effective machine learning methods (i.e., SVM, artificial neural networks, and random forests) could further differentiate non-calcified coronary plaques into fibrous and lipid plaques. All the above automatic plaque detection methods greatly improved the detection efficiency compared with the laborious manual delineation, but these methods are only effective for a specific class of coronary plaques.

Subsequently, Valencia indicated that all the coronary plaque lesions generally had certain discrepancy compared with normal arteries, although there were conspicuous morphological differences among various plaques [27]. Hereafter, Kang et al. separated coronary lesions caused by any classes of plaques from the normal arteries based on a priori knowledge that the diameter of normal artery was supposed to be gradually tapering as away from the ostium [12]. Zuluaga et al. utilized an intensity metric within a machine learning scheme to distinguish normal and abnormal cross sections [34]. They assumed that both lesions and calcifications could be considered as local outliers compared to a normal cross section. However, this method cannot distinguish the classes of different plaques, which cripple its ability of guiding risk assessment of CAD.

To handle this problem, Dey et al. proposed to quantify both calcified and non-calcified plaques using threshold segmentation, in which the scan-specific attenuation threshold for each class of plaques was automatically determined from luminal attenuation [7]. Tessmann et al. extended the detection approach for soft and calcified plaques by describing the cylinder coronary artery in cardiac CPR vessel image [25]. They integrated the multi-resolution approach into the feature extraction strategy, making it possible to increase its overall detection rate and robustness. Furthermore, Kelm et al. proposed to detect coronary stenosis in CTA caused by all classes of plaques based on radius regression with random forests [13]. However, they just mentioned adapting probability scores by two classifiers to the detection of calcified and non-calcified plaques, neglecting the detection of mixed plaques.

1.2 Problems and contribution

Although the previous methods have been widely used in detecting of coronary plaques, there are some limitations hindering their accurate clinical applications, which are summarized as follows.

(1) Most of the previous methods focus either on the detection of a specific class of coronary plaques or on the distinction between plaques and normal arteries, neglecting the classification among different classes of plaques. It is known that different classes of plaques are generally related to different severity levels of CAD. For example, non-calcified plaques take more responsibility than calcified plaques for unstable angina pectoris or non-ST-elevation myocardial infarction [5].
(2) With only intensity- or lumen diameter-based features, studies in [7, 13, 25] tried to detect and classify coronary plaques into calcified and non-calcified plaques. However, they cannot detect mixed plaques that are between calcified and non-calcified plaques in composition and morphology. Clinical trials have shown that presence of non-calcified plaques and especially mixed plaques with co-existing vulnerable plaque characteristics (low attenuation, positive remodeling, or spotty calcification) are higher risk predictors of major cardiac events on CT [23, 24], which demonstrated the importance of mixed plaques for clinical prediction of CAD.
(3) Both the feature extraction methods in [22, 31] take contextual information into account and depress the influence of image noise to some extent. However, these features only depend on the intensity differences between different objects, limiting the distinguishability of lesions (or plaques) and normal arteries. In addition, manually assigned radius used for sampling may be under- or over-estimated; thus, the features would either underestimate the lesion or bring in the interference of surrounding organs.

In this paper, we proposed an automatic multi-class coronary atherosclerosis plaque detection and classification framework, which can simultaneously detect three classes of plaques, including calcified, non-calcified, and mixed plaques. Due to the introduction of randomness in the extraction of multiple features (statistical intensity, second-order gradient, local curvature, and texture), our framework effectively increases the accuracy and robustness of multi-class plaques detection. In detail, we firstly transformed the original CTA image (in three orthographic views) into a series of transverse cross sections along the coronary centerline. Secondly,

we designed and extracted a random radial symmetry (RRS) feature vector on each cross section, which incorporated multiple contextual features of plaques and substantially augmented the training data. Finally, we fed the original feature vectors together with the augmented feature vectors into a classifier (SVM or random forests) to conduct multi-class plaque detection. The proposed framework provides a computer-aided diagnosis method for multi-class plaque detection and classification.

2 Method

As shown in Fig. 1, the proposed automatic multi-class coronary atherosclerosis plaque detection and classification framework mainly consist of three components. Firstly, we retrieved 2D transverse cross-sectional images along the given centerline from the original 3D CTA image in three orthographic views (Section 2.1). Secondly, we segmented the coronary lumen on each cross section and estimate the lumen radius by averaging over a segment of coronary artery, which is used to extract the region of interest (ROI) on the cross section (Section 2.2). Thirdly, we designed and extracted a random radius symmetry (RRS) feature vector, including the statistical intensity, second-order gradient, local curvature, and texture features. The RRS feature vector incorporated multiple descriptions within the ROI into the random strategy, greatly augmenting the training data of coronary plaques (Section 2.3). We fed the RRS feature vectors of both plaque and normal cross sections into the multi-class coronary plaque classifier, so as to recognize the non-calcified, calcified, and mixed plaques.

2.1 Transforming CTA image into cross sections

The assumption that a normal coronary has a circle-like lumen is often invalid on CTA image in three orthographic views (i.e., the coronal, sagittal, and transverse views, as shown in Fig. 2a), because this visualization does not take vessel-specific observation into account. To solve this problem, we transformed the original CTA image into a series of transverse cross sections along the given centerline. Centerlines are defined as the medial axes along the coronary arteries, commonly used to handle the topology of corresponding arteries (e.g., the top left inset of Fig. 1). In the retrieved cross sections (Fig. 2b), the normal artery generally has circle-like lumen, while the plaque artery does not, which differentiate normal and plaque arteries effectively [28]. The transformation consists of coordinate correspondence, image registration, and linear interpolation.

Given a point on the centerline is located at $\mathbf{c} = (c_x, c_y, c_z)$ in the original coordinate system before transformation, the corresponding transverse cross section is sliced along the centerline tangent direction. We denote the centerline tangent direction as the normal vector $\mathbf{m} = (m_x, m_y, m_z)$ of the transverse plane, which is acquired by forward difference between two consecutive centerline points. We establish a coordinate system, selecting the retrieved cross section as xOy plane and the centerline crosses the origin. Thus, the new normal vector is $\mathbf{n} = (0, 0, 1)$. Therefore, the registration of two cross sections before and after transformation reduces to the registration of two normal vectors $\boldsymbol{m}$ and $\boldsymbol{n}$ (Fig. 3).

The transformation for registration of $\boldsymbol{m}$ and $\boldsymbol{n}$ can be decomposed into translation and rotation. We first translate the centerline point $\boldsymbol{c}$ to the origin of coordinates, which is identical for two systems before and after transformation (Fig. 3a). Then, we rotate $\boldsymbol{m}$ about x-axis to its projection $\boldsymbol{m}_{xz}$ on the xOz plane. The rotation angle from $\boldsymbol{m}$ to $\boldsymbol{m}_{xz}$ is denoted as φ (Fig. 3b). Subsequently, we rotate the vector $\boldsymbol{m}$ from $\boldsymbol{m}_{xz}$ about y-axis to $\boldsymbol{n}$. The rotation angle from $\boldsymbol{m}_{xz}$ to $\boldsymbol{n}$ is denoted as θ. Thus, the rotation from $\boldsymbol{m}$ to $\boldsymbol{n}$ can be formulated as

$$[0, 0, 1, 1]^T = R_x R_y [m_x, m_y, m_z, 1]^t \quad (1)$$

where $R_x = \begin{bmatrix} 1 & 0 & 0 & 0 \\ 0 & \cos(\varphi) & -\sin(\varphi) & 0 \\ 0 & \sin(\varphi) & \cos(\varphi) & 0 \\ 0 & 0 & 0 & 1 \end{bmatrix}$ and $R_y = \begin{bmatrix} \cos(\theta) & 0 & -\sin(\theta) & 0 \\ 0 & 1 & 0 & 0 \\ \sin(\theta) & 0 & \cos(\theta) & 0 \\ 0 & 0 & 0 & 1 \end{bmatrix}$, denoting the rotation parameter matrices about x-axis and y-

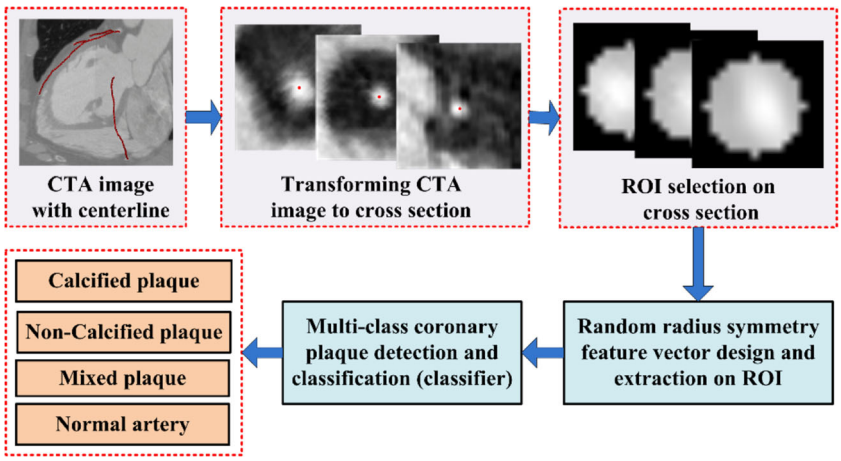

Fig. 1 Workflow of the proposed automatic multi-class coronary atherosclerosis plaque detection and classification framework

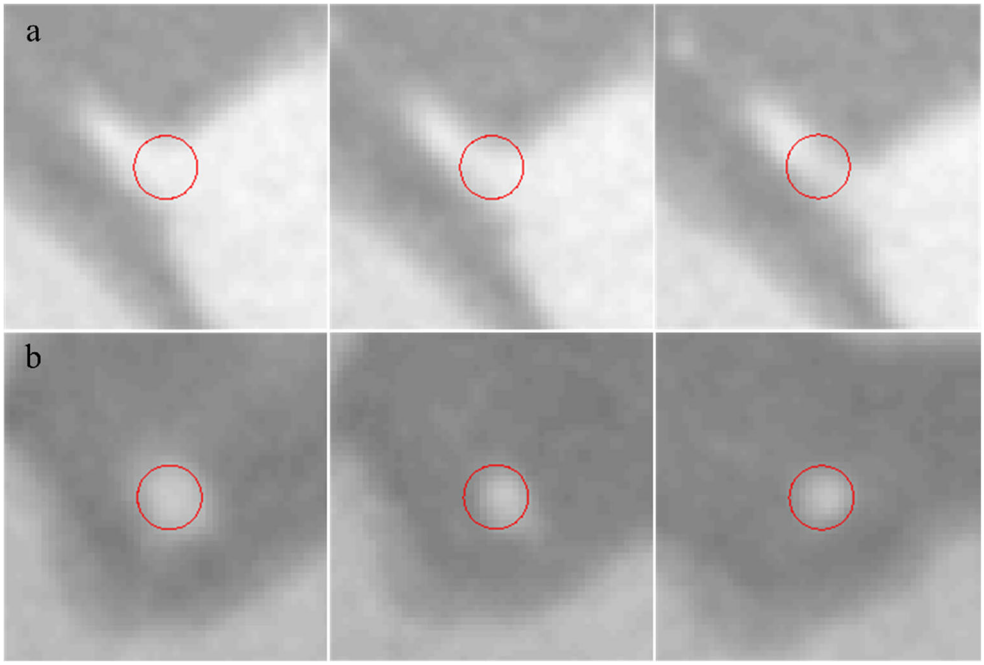

Fig. 2 Two types of 2D images with the same ROI areas and radii (5 pixels). **a** The axial images normal to z-axis. **b** The transverse cross sections normal to the centerline

axis, respectively. Given each pair of normal vectors $\boldsymbol{m}$ and $\boldsymbol{n}$, we can readily obtain the two angles φ and θ, then compute the rotation parameter matrices R_x and R_y. With these two matrices, we can retrieve the cross section from the original CTA image and align it with xOy plane. We assume the coordinate of a point on the retrieved cross section is $(x^{'}, y^{'}, 0)$ and that of the corresponding point on the original transverse image is (x, y, z). The transformation formula is given as

$$[x, y, z, 1]^T = [c_x, c_y, c_z, 0]^T + R_y^{-1} R_x^{-1} \left[x^{'}, y^{'}, 0, 1\right]^T \quad (2)$$

Lastly, linear interpolation is used to calculate the intensity of pixels in the cross section. For each centerline point, a transverse cross-sectional image is calculated along the given coronary centerline.

2.2 Selecting ROIs on cross sections

Figures 1 and 3 show that the coronary lumen is located in the center and covers only a part of the cross-section image. Besides coronary artery, there is strong interfering information from myocardium and other organs, which make it inappropriate to detect coronary plaques from the entire cross-section image. Therefore, it is necessary to select the ROIs (i.e., the coronary lumen) before plaque detection and classification. We roughly segmented the coronary lumen by modified level sets method in the first place. Then, we estimated the radius of each cross section by averaging over a segment of coronary artery. Finally, the estimated radius was used to extract the ROI on each cross section (Fig. 4).

Coronary lumen varies widely in normal and plaque arteries, and among different classes of plaques. For example,

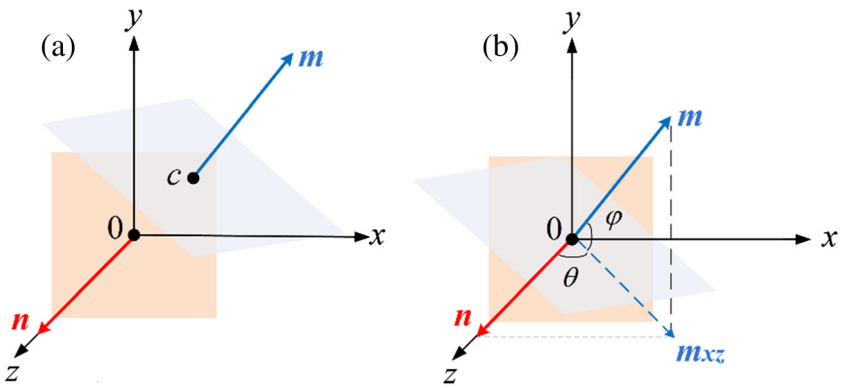

Fig. 3 Coordinate transformation and registration. **a** The original two systems before translation. **b** The two systems after translating the centerline point $\boldsymbol{c}$ to the origin of coordinates

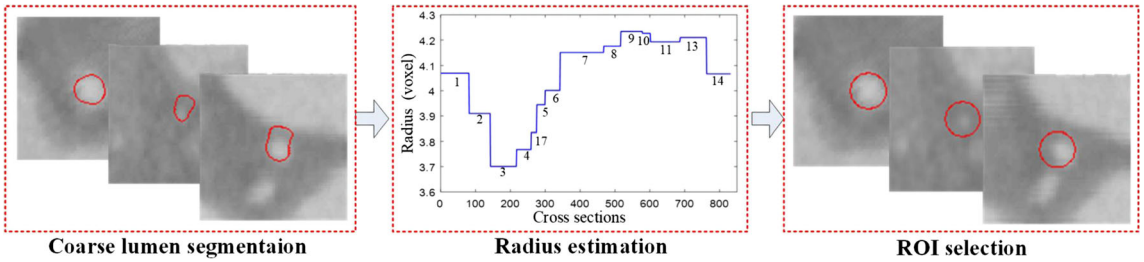

Fig. 4 Extraction of ROIs on cross sections. The left inset shows the coarse segmentation of coronary lumens (delineated with red lines) by modified level sets method. The middle inset shows the estimation of the mean radii of different segments of coronary artery (1-17). The right inset shows the selected ROIs (delineated with red lines) with the estimated radii (color figure online)

coronary lumen of calcified atherosclerosis plaque is larger than the normal one, while that of non-calcified plaque seems disconnected due to the low intensity in the CTA image. Because of these distortions of the coronary lumen, most segmentation methods failed to select accurate ROIs on cross-section images. Recently, Li et al. proposed the distance regularized level set evolution (DRLSE) method, in which they modified the conventional level set formulation by maintaining the regularity of the level set function during evolution [16]. Since DRLSE turned out to be effective on medical images, we applied it to the coarse segmentation of coronary lumen on cross-section images. With proper initialization, most of the coronary lumens could be segmented in the cross-section image. However, there were still some coronary lumens under-segmented or over-segmented as shown in Fig. 4 (left inset). Thus, the result of lumen segmentation by DRLSE can only act as an initial estimation of coronary lumen region, which supplied a coarse contour for the subsequent radius estimation.

On each cross-section image, the initial radius is computed by considering the farthest and nearest points on the surrounding contour to the centerline point. Considering the under-segmented and over-segmented issues in the distorted cross sections, it is practical to further average the initial radii along a segment of coronary artery, in which the partition of each segment referred to the modified 17 segments of the AHA reporting system [2]. Thus, the lumen radii of a series of cross sections may be identical if they lie in the same segment of coronary artery. This is rational because the size of each segment of coronary artery changes slightly. Moreover, this strategy greatly depresses the instability of initial radius estimation caused by the inaccurate coarse lumen segmentation. Based on the estimated radius, we select a disk on each cross section as the ROI for subsequent plaque detection and classification.

2.3 Designing and extracting RRS feature vector

Feature extraction is crucial for coronary plaque detection via machine learning-based methods. Spatial context features are specially designed for the lesion segmentation in human abdomen and retina, which have become a group of effective features due to the integration of multiple information [17, 18]. Motivated by the idea of spatial context features, we designed a random radius symmetry (RRS) feature vector in our framework. We firstly standardized the cross sections within the ROIs, such that we could establish the anatomical correspondence between feature vectors and different coronary plaques. Then, we extracted the RRS feature vector on the standardized cross sections, which has the ability to augment the original data by introducing little perturbation on the initial sampling angles.

2.3.1 Image standardization

Image standardization within ROIs of cross sections consisted of two phases. In the first phase, adaptive radii were selected on cross sections with different resolutions or on different segments of coronary artery, which was accomplished by the radius estimation during the ROI selection (in Section 2.2). In the second phase, target angles for different plaques were set based on the intensity variation within the corresponding ROI (Fig. 5).

We partitioned each ROI into eight sectors with identical angle intervals ($\pi/4$) and then calculated the mean intensity in each sector (Fig. 5a). We obtained the target angle ψ_0 of each ROI via finding the sector with the maximum mean intensity. The confidence value ζ for the target angle ψ_0 was given by the difference between the maximum and minimum mean intensities among the eight sectors. To avoid accidentally partitioning a region with high intensity into two sectors, we shifted the polar grid consisting of the eight sectors by an interval of $\pi/12$. As shown in Fig. 5a, the final ζ was the maximum confidence value at different shifting angles. The optimal ψ_0 was obtained by maximizing the confidence values at different shifting angles as follows:

$$\psi_0 = \mathrm{argmax}_{i\in\{0,\pi/12,\pi/6\}}\ \zeta_i \tag{3}$$

Because of the rotation invariance, we just shifted the initial polar grid ($i = 0$) by $\pi/12$ and $\pi/6$. If the final value of ζ was less than an empirical threshold, we directly assigned the target angle ψ_0 as zero, which generally corresponds to the cross sections of normal arteries. To clarify the anatomical correspondence between feature vectors and different coronary

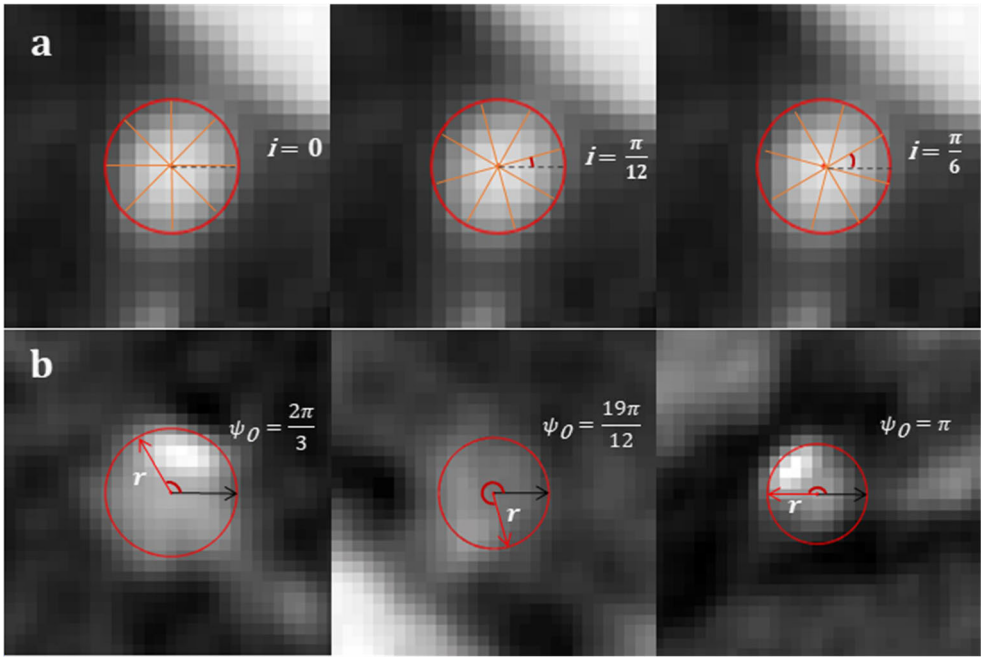

Fig. 5 Image standardization within ROIs of cross sections. **a** ROI was partitioned into eight sectors at three different polar grids. **b** Examples of image standardization for different classes of coronary plaques (with adaptive ROI radius r and target angle ψ_0)

plaques, we provided examples of random selected cross sections of calcified, non-calcified, and mixed plaques in Fig. 5b.

2.3.2 RRS feature vector

Unlike the previous spatial context features, the proposed random radius symmetry (RRS) feature vector incorporated image gradient, curvature, and textural features into the statistical intensity features, increasing the description ability of plaques and normal coronaries. Moreover, in order to augment the training data, randomness was also introduced into the selection of the initial sampling angle. We sampled multiple 3×3 patches within the ROI on each cross section. The distribution of the patch centers is shown in Fig. 6, determined by the different radii from the center and the side corresponding to the target angle ψ_0.

Specifically, as shown in Fig. 6a, we partitioned the ROI into N concentric circles with radii of $\frac{1}{N}r, \frac{1}{N}r, \cdots, r$, respectively, where r is the estimated radius from ROI selection. On the ith circle with radius $R_i = \frac{i}{N}r$ ($i = 1, 2, \ldots, N$), we sampled M_i patches with identical angular intervals $\Delta\psi_i = 2\pi/M_i$ (Fig. 6b). We randomized the angle $\psi_{i,1}$ between the radius corresponding to the first sample point on the ith circle and the target angle side. The radian measure of $\psi_{i,1}$ lies in the interval $[0, \Delta\psi_i)$ rather than $[0, 2\pi)$, due to the consideration of anatomical correspondence. Thus, the positions of sample patches in polar coordinates on the ith circle can be formulated as

$$(R_i, \psi_i) = \left\{ \left(\frac{i}{N}r, \psi_0 + \psi_{i,1}\right), \left(\frac{i}{N}r, \psi_0 + \psi_{i,1} + \Delta\psi_i\right), \cdots, \left(\frac{i}{N}r, \psi_0 + \psi_{i,1} + (M_i - 1)\Delta\psi_i\right) \right\} \quad (4)$$

where $\Delta\psi_i = 2\pi/M_i$ is the interval between two adjacent patches on the ith circle.

The proposed sampling strategy can fully exploit the image information from different patches with the randomness of initial angle $\psi_{i,1}$ ($i = 1, 2, \ldots, N$) on each circle, which effectively augments the feature data for subsequent plaque detection and classification. This strategy is necessary when coronary CTA images, especially the plaque lesion images, are not sufficient. It should be noted that the hyper-parameters N and M_i are empirically assigned, which depend on the area of ROIs as well as computational capacity. Once the positions of all the patches were acquired in an ROI, we could compute the statistical intensity, second-order gradient, local curvature, and textural features on each patch. Then, all the features in this ROI were combined one by one to construct a RRS feature vector covering all the $\sum_{i=1}^{N} M_i$ patches. In each patch, the four types of features were calculated as follows:

Statistical intensity The mean μ and variance σ^2 were readily obtained from the intensities of the nine pixels in each 3×3 patch. Based on these two low-order moment features, we could compute the high-order

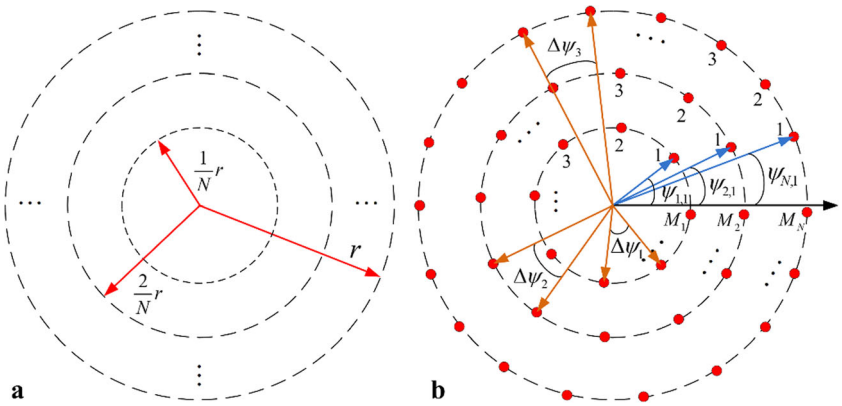

Fig. 6 The sampling strategy of the random radius symmetry (RRS) feature vector. **a** The partition of ROI into N concentric circles. **b** The samping with identical angular intervals on each concentric circle

statistical features including the skewness ϑ and kurtosis κ, which are given as

$$\begin{cases} \vartheta = E\left[\left(\dfrac{I(x',y')-\mu}{\sigma}\right)^3\right] \\ \kappa = E\left[\left(\dfrac{I(x',y')-\mu}{\sigma}\right)^4\right] \end{cases} \tag{5}$$

where $I(x',y')$ is the intensity of the pixel (x',y') in the retrieved cross-section image.

Second-order gradient The second-order gradient features for each pixel are formulated by the Hessian matrix:

$$H(x',y') = \begin{bmatrix} \dfrac{\partial^2}{\partial x'^2} I(x',y') & \dfrac{\partial^2}{\partial x'\partial y'} I(x',y') \\ \dfrac{\partial^2}{\partial y'\partial x'} I(x',y') & \dfrac{\partial^2}{\partial y'^2} I(x',y') \end{bmatrix} \tag{6}$$

where each element of the Hessian matrix in Eq. (6) is a second-order gradient. Considering the equivalence of $\frac{\partial^2}{\partial x'\partial y'} I(x',y')$ and $\frac{\partial^2}{\partial y'\partial x'} I(x',y')$, we picked $\frac{\partial^2}{\partial x'^2} I(x',y')$, $\frac{\partial^2}{\partial x'\partial y'} I(x',y')$, and $\frac{\partial^2}{\partial y'^2} I(x',y')$ as the three second-order gradient features. In each patch, the values of the three second-order gradient features were averaged.

Local curvature The curvature is formulated by the hybrid of first- and second-order gradients of image intensity as follows [31]:

$$C(x',y') = \frac{\left[1+\left(\frac{\partial}{\partial x'} I\right)^2\right]\frac{\partial^2}{\partial y'^2} I - 2\frac{\partial}{\partial x'} I \frac{\partial}{\partial y'} I \frac{\partial^2}{\partial x'\partial y'} I + \left[1+\left(\frac{\partial}{\partial y'} I\right)^2\right]\frac{\partial^2}{\partial x'^2} I}{2\left[1+\left(\frac{\partial}{\partial x'} I\right)^2 + \left(\frac{\partial}{\partial y'} I\right)^2\right]} \tag{7}$$

where I is short for $I(x',y')$. In each patch, the local curvature feature was the average of the curvature values of the nine pixels.

Local texture Local texture feature was obtained based on texture maps filtered by 2D Gabor banks at 90° orientation, which was calculated as follows [17]:

$$G(x',y') = \zeta g\left(\zeta\left(x'\cos\alpha + y'\sin\alpha\right), \zeta\left(-x'\sin\alpha + y'\cos\alpha\right)\right) \tag{8}$$

where $g(u,v) = \frac{1}{2\pi\sigma_u\sigma_v}\exp\left[-\frac{1}{2}\left(\frac{u^2}{\sigma_u^2}+\frac{v^2}{\sigma_v^2}\right) + 2\pi j(Wu+Vv)\right]$ is the Gaussian function with the shifting parameters W and V in the frequency domain; $\alpha = \frac{\pi}{2}$ is the orientation of Gabor banks; and $\zeta = \left(\frac{F_h}{F_l}\right)^{1/3}$ is the scaling factor with F_h and F_l as the frequency range parameters of filter back. Similarly, the local texture feature was averaged in the patch.

There were nine features in each patch, including four statistical intensity features, three second-order gradient features, one local curvature, and one local texture feature. After traversing all the patches in the ROI in each cross-section image, the RRS feature vector was assembled with $9\cdot\sum_{i=1}^{N} M_i$ features. Subsequently, we fed the RRS feature vectors of both the plaque and normal cross sections into the multi-class coronary plaque classifier to detect the calcified, non-calcified, and mixed plaques.

3 Results

3.1 Dataset and evaluation methodology

The datasets adopted in this paper were from Rotterdam Coronary Artery Evaluation Dataset, which were designed for coronary stenosis detection and plaque analysis [14]. This dataset contains 18 CTA images with manually extracted centerlines by three experts. Each coronary centerline point in CTA image had been labeled as having atherosclerotic plaque (including calcified, non-calcified, and mixed plaques) or not. After cross-section retrieval along the centerline and ROI selection, there were totally 1786 cross sections having

atherosclerotic plaques (729 non-calcified plaques, 511 calcified plaques, and 546 mixed plaques) and 14,628 normal cross sections. The size of the cross section was 51×51 in pixel. During the RRS feature vector extraction, we tried many combinations of N and M_i ($i = 1, 2, \ldots, N$) and concluded that the optimal trade-off between computation and accuracy was $N = 3$, $M_1 = 8$, $M_2 = 12$, and $M_3 = 18$. Thus, in each cross section, there were 38 patches in total, and each RRS feature vector was assembled with $9 \times 38 = 342$ features. According to Section 2.3, the radian measure of the initial angle $\psi_{i,1}$ on each concentric circle lay in the interval $[0, \Delta\psi_i)$ ($i = 1, 2, 3$) with $\Delta\psi_1 = \pi/4$, $\Delta\psi_2 = \pi/6$, and $\Delta\psi_3 = \pi/9$. The angular randomization step was $\pi/36$ for all the three initial angles, so that we could acquire as much as $9 \times 6 \times 4 = 216$ different RRS feature vectors in each cross section.

The proposed framework has two goals: plaque detection and classification. After plaque detection, we need to further classify all the coronary plaques into calcified, non-calcified, and mixed plaques. Thus, four quantitative evaluation indices including precision, recall, F_1 score, and accuracy were employed to evaluate the performance of our framework. The classifier we used for coronary plaque detection and classification was support vector machine (SVM) with Gaussian kernel due to its superiority for small samples. The penalty coefficient C and kernel parameter σ were 10 and 0.6, respectively. In all experiments, we randomly set 80% of the RRS feature vectors as the training data and the remaining 20% of the RRS feature vectors as the testing data. The amount of normal data was determined by trial-and-error to eliminate the training error. All the experiments were run with 10-fold cross-validation.

3.2 Cross-section validation

To test the performance of plaque detection in cross sections over that in original CTA images in three orthogonal views, we sliced the axial images from 3D CTA image along z-axis, which was equivalent to those along x-axis and y-axis. No matter which axis we choose, the slicing angle was fixed and the axial images was impossible to be normal to the coronary centerline. We set the radii for both the transverse cross sections along the centerline and the axial images normal to z-axis as 5 in pixel. Then, we carried out the RRS feature vector extraction on the two types of 2D images in the circular areas with radius of 5 pixels (Fig. 2).

The quantitative results are given in Table 1. The F_1 scores of non-calcified and mixed plaques on cross sections are higher than those in the original axial images. It is also observed that the F_1 score of calcified plaques in the axial images are better than that in the cross sections. Nevertheless, the average precision, recall, F_1 score, and accuracy of the proposed framework in cross sections are higher than those in the axial images, demonstrating the feasibility and effectiveness of plaque detection in cross sections.

3.3 ROI selection validation

After validating the effectiveness of plaque detection in cross sections, it is imperative to test the performance of the ROI section. The estimated radii in different coronary segments (17-segments) ranged from 3.1 to 5.7 in pixel, i.e., the sampling area in our framework was adaptively determined for each cross sections. In control experiments, we fixed the radius of ROI as 3, 4, 5, and 6 pixels, respectively. Comparison between sampling with adaptive radius and fixed radius was given in Table 2, where the average precision, recall, F_1 score, and overall accuracy were calculated. With the increase of radius, most of the quantitative indices peak at radius of 4 pixels. The proposed ROI selection with adaptive radius prevail in terms of average recall, F_1 score, and overall accuracy. Thus, the superiority of the proposed ROI selection was demonstrated.

3.4 RRS feature vector validation

In Sections 3.2 and 3.3, we demonstrated that the cross-section transformation and ROI selection in our framework improved the performance of plaque detection. However, the detection ability for all classes of plaques should be improved, as indicated by the relatively low F_1 score and accuracy. To handle these problems, we randomly collected up to nine folds of different combinations of initial angles $\Delta\psi_i$ ($i = 1, 2, 3$) and extracted the same amount of RRS feature vectors in each cross section. Therefore, we boosted the original 1786 plaque features vectors up to 17,820 ones. The feature vectors of normal arteries could also be boosted with the same way if necessary.

The results with different folds of augmenting training data are given in Table 3, where the average precision, recall, F_1 score, and overall accuracy were calculated. In our experiment, the testing data were also augmented to maintain the ratio of training and testing data (80 vs. 20%). With the increase of training data, the detection rate for coronary plaques increases, which reaches the maximum when 8-fold augmentation of training data are used for SVM training. For example, the average precision is $88.1 \pm 2.1\%$ before augmentation and grows dramatically to $92.6\% \pm 1.9\%$ after 8-fold augmentation. This also lead to great improvement of F_1 score and accuracy with the augmentation of training data, which are much higher compared with the plaque detection without data augmentation.

3.5 Results of the proposed framework

To further validate the proposed framework, we conducted two comparative experiments, including using different

Table 1 Results of plaque detection in axial images and cross sections

		Pre (%)	Rec (%)	F_1 (%)	Acc (%)
Axial images	Non-calcified	*87.5 ± 3.0*	92.0 ± 2.4	89.7 ± 2.6	–
	Calcified	*83.6 ± 3.7*	*91.1 ± 2.8*	*87.6 ± 3.1*	–
	Mixed	88.1 ± 3.8	*85.0 ± 3.6*	86.5 ± 3.7	–
	Mean	86.4 ± 3.3	89.3 ± 2.9	87.8 ± 3.2	87.1 ± 2.1
Cross sections	Non-calcified	85.0 ± 3.3	*97.4 ± 0.9**	*90.8 ± 2.1**	–
	Calcified	83.2 ± 3.3	90.6 ± 3.5	86.7 ± 3.4	–
	Mixed	*94.2 ± 2.5**	83.9 ± 3.4	*88.8 ± 2.0**	–
	Mean	*87.5 ± 2.1**	*90.6 ± 2.6**	*88.8 ± 2.9**	*88.7 ± 1.2**

The italicized entries are the highest values of corresponding indices among the two groups. Precision, recall, F_1 score, and accuracy are abbreviated as Pre, Rec, F_1, and Acc, respectively

*The indices having statistically significant differences among the two groups

feature vectors and classifiers. We noticed that both Tessmann et al. [25] and Zuluaga et al. [34] employed intensity metrics feature vector. Thus, we first compared our proposed RRS feature vector with the feature vector only using intensity metrics, including mean, variance, skewness, and kurtosis. In addition, we tested the influence of different classifiers: SVM and random forests (RF), as the latter was another state-of-the-art machine learning method. The precision and recall for the three classes of coronary plaques (non-calcified, calcified, and mixed plaques) and the overall estimation (F_1 score and accuracy) are given in Fig. 7.

The four evaluation indices (average precision, recall, F_1 score, and accuracy) for SVM classifier are almost monotonically increased no matter with the proposed RRS or only with the intensity feature vector. The similar trend can also be observed in the precision of RF classifier. Nearly for all the augmentation folds (from 1 to 9), the evaluation indices of our RRS feature vector are higher than those of intensity feature vector, while the SVM classifier are better than the RF classifiers. To show the performance differences clearly, we highlighted the results of the SVM and RF classifiers after 8-fold augmentation with both feature vectors in Table 4.

All the four indices (precision, recall, F_1 score, and accuracy) of SVM with the RRS feature vector are higher than those of SVM with the intensity feature vector. Similarly, RF with the RRS feature vector outperforms RF with the intensity feature vector. It indicates that the performance of the RRS feature vector is superior to the intensity feature vector. On the other hand, almost all the indices of SVM classifier with the RRS feature vector are higher than RF classifier with the same feature vector. The average precision and recall of the SVM classifier with RRS feature vector are 92.6 ± 1.9 and 94.3 ± 2.1%, respectively, while those of RF are 88.4 ± 2.9 and 79.4 ± 3.0%, respectively. The results demonstrate that the SVM classifier is more suitable for the task of multi-class plaque detection and classification.

Table 2 Results of plaque detection in cross sections with fixed and adaptive radii

	r	Pre (%)	Rec (%)	F_1 (%)	Acc (%)
Fixed	3	86.2 ± 2.9	87.6 ± 2.1	86.8 ± 2.4	86.8 ± 1.1
	4	*88.3 ± 3.0*	90.3 ± 2.6	89.1 ± 1.7	88.9 ± 1.0
	5	87.5 ± 2.1	90.6 ± 2.6	88.8 ± 2.9	88.7 ± 1.2
	6	87.3 ± 2.3	91.4 ± 2.7	88.7 ± 2.1	87.5 ± 1.4
Adaptive	–	88.1 ± 2.1	*91.5 ± 2.3*	*89.5 ± 2.5*	*89.2 ± 1.3*

The italicized entries are the highest values of corresponding indices among the groups. Precision, recall, F_1 score, and accuracy are abbreviated as Pre, Rec, F_1, and Acc, respectively

4 Discussion

The proposed multi-class coronary plaque detection and classification framework is based on the assumption that the corresponding centerline has been extracted. Actually, centerlines are often used in the topological description of complex vascular networks [32, 33]. Specifically, the extraction of coronary centerline before lumen segmentation has been widely

Table 3 Plaque detection with different folds of augmenting training data

Fold	Pre (%)	Rec (%)	F_1 (%)	Acc (%)
1	88.1 ± 2.1	91.5 ± 2.3	89.5 ± 2.5	89.2 ± 1.3
2	89.8 ± 2.6	92.5 ± 2.6	91.0 ± 2.4	91.0 ± 1.7
3	91.2 ± 2.4	93.3 ± 2.3	92.1 ± 2.1	92.1 ± 1.4
4	91.4 ± 2.0	94.1 ± 1.7	92.6 ± 1.8	92.7 ± 0.8
5	91.5 ± 2.0	93.5 ± 2.1	92.4 ± 1.9	92.7 ± 1.1
6	92.0 ± 1.9	94.0 ± 2.0	92.8 ± 1.9	93.0 ± 1.1
7	91.5 ± 2.0	93.4 ± 2.2	92.3 ± 2.0	92.8 ± 0.8
8	*92.6 ± 1.9*	*94.3 ± 2.1*	*93.3 ± 1.9*	*93.5 ± 1.0*
9	91.9 ± 1.9	93.5 ± 2.2	92.6 ± 2.0	93.0 ± 1.6

The italicized entries are the highest values of corresponding indices among different groups. Precision, recall, F_1 score, and accuracy are abbreviated as Pre, Rec, F_1, and Acc, respectively

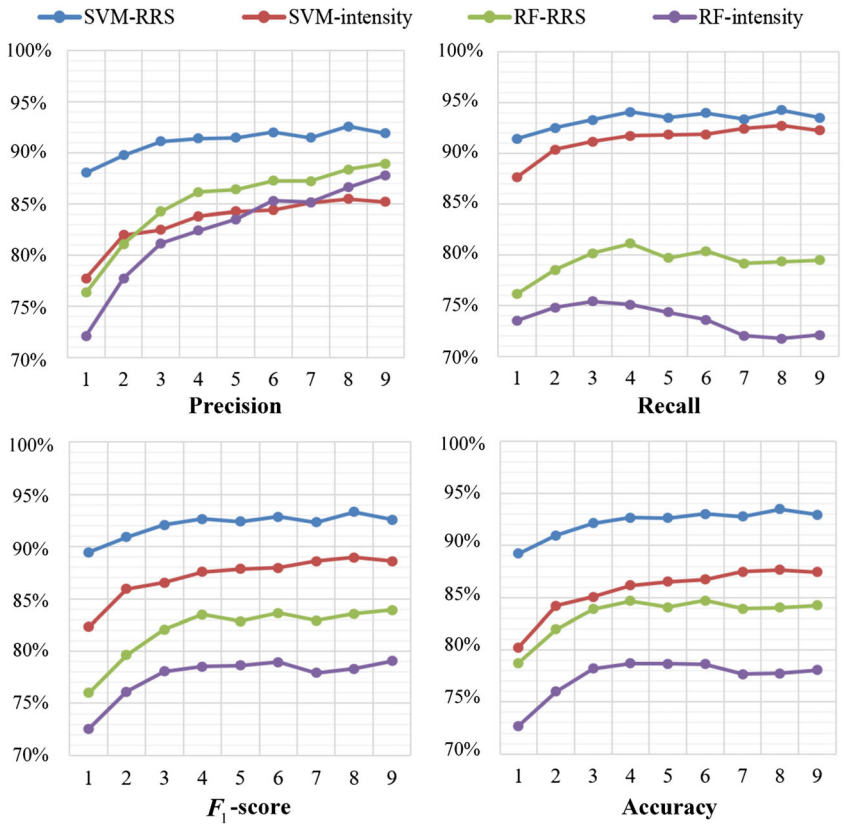

Fig. 7 Comparison with other feature vectors and classifiers. The horizontal line represents the folds of data augmentation

investigated [3, 30]. This paper mainly focuses on the multi-class detection of plaques; thus, we did not discuss the influence of centerline extraction, however, which will be incorporated in the future.

To transform the original CTA images into cross sections, we had to slice the CTA volumetric image transversely along the centerline and fit the sliced images into a new coordinate system, which formed the so-called cross sections. The

Table 4 Performance of plaque detection with different classifiers and feature vectors after 8-fold data augmentation

		Pre (%)	Rec (%)	F_1 (%)	Acc (%)
SVM with RRS feature vector	Non-calcified	91.7 ± 1.9	*98.2 ± 1.1*	*94.8 ± 1.4*	–
	Calcified	*89.2 ± 1.7*	94.5 ± 2.4	92.0 ± 2.0	–
	Mixed	*96.8 ± 2.0*	89.7 ± 2.9	93.1 ± 2.3	–
	Mean	*92.6 ± 1.9*	*94.3 ± 2.1*	*93.3 ± 1.9*	*93.5 ± 1.0*
SVM with intensity feature vector	Non-calcified	88.9 ± 2.1	96.2 ± 1.4	92.4 ± 1.7	
	Calcified	82.6 ± 1.8	93.6 ± 2.5	87.7 ± 2.1	
	Mixed	85.0 ± 2.2	88.5 ± 3.3	86.7 ± 2.6	
	Mean	85.5 ± 2.0	92.8 ± 2.4	89.0 ± 2.1	87.7 ± 0.8
RF with RRS feature vector	Non-calcified	*95.1 ± 1.8*	80.7 ± 2.9	87.4 ± 2.2	–
	Calcified	87.9 ± 3.2	78.2 ± 3.6	82.8 ± 3.4	–
	Mixed	82.2 ± 3.7	79.1 ± 2.5	80.6 ± 3.0	–
	Mean	88.4 ± 2.9	79.4 ± 3.0	83.6 ± 2.9	84.1 ± 1.1
RF with intensity feature vector	Non-calcified	95.0 ± 1.6	78.7 ± 2.5	86.1 ± 2.0	–
	Calcified	82.4 ± 2.2	76.5 ± 2.3	79.4 ± 2.3	–
	Mixed	82.4 ± 3.9	60.1 ± 3.1	69.5 ± 3.5	–
	Mean	86.6 ± 2.6	71.8 ± 2.7	78.3 ± 2.6	77.8 ± 1.3

The italicized entries are the highest values of corresponding indices among different groups. Precision, recall, F_1 score, and accuracy are abbreviated as Pre, Rec, F_1, and Acc, respectively

alignment between the axial image in the original coordinate system and the cross section in the new coordinate system was reduced to the registration between their corresponding normal vectors $\boldsymbol{m}$ and $\boldsymbol{n}$. Since $\boldsymbol{n}$ is constantly equal to (0, 0, 1), the accuracy of estimation of $\boldsymbol{m}$ determines the precision of transformation. In our framework, $\boldsymbol{m}$ was acquired by forward difference of centerline points, which could be improved by more sophisticated fitting method in the future. Another factor affecting the transformation is the interpolation strategy, e.g., the employed linear interpolation in our framework is more effective than nearest neighbor interpolation.

The proposed random radius symmetry (RRS) feature vector brought the randomness to the multiple contextual features of coronary plaques in the ROI in each cross section, which greatly improved the detection rates of all three classes of plaques. A critical issue of RRS feature vector extraction is how to determine the number of patches, which generally depends on the radius of ROI. We need to guarantee that the number of patches is sufficient to sample as many different locations as possible, while any two sampling patches cannot be overlapped with each other. Moreover, the distribution of the patches should be approximately uniform in the ROI. Taking these two factors and the experimented values of radii into account, we sampled the patches on three concentric circles in the ROI of each cross section and acquired 8, 12, and 18 patches on each circle, respectively.

There are two limitations in our present work that will be addressed in the future. The first one is that we improved the detection rate of different classes of coronary plaques at the expense of computation time. Compared with the original data without augmentation, the training time on the augmented data was increased dramatically, especially for the SVM classifier with Gaussian kernel. The second limitation is that the detection and classification of plaques were only based on single cross section. Generally, a plaque spans across several cross sections and leads to the occurrence of stenosis. Therefore, we will take the detection results on neighboring cross sections into consideration and create an integrated detection and classification framework in the future.

5 Conclusions

In conclusion, we proposed an automatic multi-class coronary atherosclerosis plaque detection and classification framework. Firstly, we retrieved 2D transverse cross-section images from the original 3D CTA image along the given centerline. Secondly, we coarsely segmented the coronary lumen, estimated the lumen radius, and extracted the ROI on the cross section. Thirdly, we designed and extracted a random radius symmetry (RRS) feature vector, which incorporated multiple contextual features and greatly augmented the training data of coronary plaques. The results validated the effectiveness of plaque detection with RRS feature vector after ROI selection in cross sections. Moreover, compared with previous intensity feature vectors and other classifiers, the SVM classifier with the proposed RRS feature vector performs the best in terms of precision, recall, F_1 score, and accuracy. The proposed framework provides a computer-aided diagnostic method for multi-class plaque detection and classification.

Acknowledgements The authors also would like to thank Dr. Muhan Liu for his assistance in polishing the manuscript.

Funding information This work was partly supported by the National Key R&D Program of China under Grant No. 2016YFC1300300; the National Natural Science Foundation of China under Grant Nos. 61601363, 61701403, 61401264, 11571012, 81530058; the Natural Science Research Plan Program in Shaanxi Province of China under Grant Nos. 2017JQ6017, 2017JQ6006, 2015JM6322, and 2015JZ019; and the Scientific Research Foundation of Northwest University.

Compliance with ethical standards

Conflict of interest The authors declare that they have no conflict of interest.

Ethical approval All the CTA data are obtained from public database. No human/animal experiments are involved in this paper.

References

1. Acharya UR, Mookiah MRK, Sree SV, Afonso D, Sanches J, Shafique S, Nicolaides A, Pedro LM, Fernandes e Fernandes J, Suri JS (2013) Atherosclerotic plaque tissue characterization in 2D ultrasound longitudinal carotid scans for automated classification: a paradigm for stroke risk assessment. Med Biol Eng Comput 51: 513–523 Doi https://doi.org/10.1007/s11517-012-1019-0
2. Austen WG, Edwards JE, Frye RL, Gensini GG, Gott VL, Griffith LS, McGoon DC, Murphy ML, Roe BB (1975) A reporting system on patients evaluated for coronary artery disease. Report of the Ad Hoc Committee for Grading of Coronary Artery Disease, Council on Cardiovascular Surgery, American Heart Association. Circulation 51:5–40
3. Chen Y, Zhang Y, Yang J, Cao Q, Yang G, Chen J, Shu H, Luo L, Coatrieux J-L, Feng Q (2016) Curve-like structure extraction using minimal path propagation with backtracking. IEEE Trans Image Process 25:988–1003. https://doi.org/10.1109/tip.2015.2496279
4. Cruz-Aceves I, Hernandez-Aguirre A, Ivvan Valdez S (2016) On the performance of nature inspired algorithms for the automatic segmentation of coronary arteries using Gaussian matched filters. Appl Soft Comput 46:665–676. https://doi.org/10.1016/j.asoc.2016.01.030
5. Dalager MG, Bottcher M, Thygesen J, Andersen G, Botker HE (2015) Different plaque composition and progression in patients with stable and unstable coronary syndromes evaluated by cardiac CT. Biomed Res Int 2015:401357–401359. https://doi.org/10.1155/2015/401357
6. de Graaf MA, Broersen A, Kitslaar PH, Roos CJ, Dijkstra J, Lelieveldt BPF, Jukema JW, Schalij MJ, Delgado V, Bax JJet al (2013) Automatic quantification and characterization of coronary atherosclerosis with computed tomography coronary angiography: cross-correlation with intravascular ultrasound virtual histology. Int

J Cardiovasc Imaging 29: 1177–1190 Doi https://doi.org/10.1007/s10554-013-0194-x

7. Dey D, Cheng VY, Slomka PJ, Nakazato R, Ramesh A, Gurudevan S, Germano G, Berman DS (2009) Automated 3-dimensional quantification of noncalcified and calcified coronary plaque from coronary CT angiography. J Cardiovasc Comput Tomogr 3:372–382. https://doi.org/10.1016/j.jcct.2009.09.004
8. Dhanaseelan R, Jeya Sutha M (2017) Diagnosis of coronary artery disease using an efficient hash table based closed frequent itemsets mining. Med Biol Eng Comput 56:749–759. https://doi.org/10.1007/s11517-017-1719-6
9. Fuchs TA, Fiechter M, Gebhard C, Stehli J, Ghadri JR, Kazakauskaite E, Herzog BA, Husmann L, Gaemperli O, Kaufmann PA (2013) CT coronary angiography: impact of adapted statistical iterative reconstruction (ASIR) on coronary stenosis and plaque composition analysis. Int J Cardiovasc Imaging 29:719–724. https://doi.org/10.1007/s10554-012-0134-1
10. Guaricci AI, Pontone G, Brunetti ND, De Rosa F, Montrone D, Guglielmo M, Mushtaq S, Fusini L, Maffei E, Cademartiri Fet al (2016) The presence of remodeled and mixed atherosclerotic plaques at coronary ct angiography predicts major cardiac adverse events—the CAFE-PIE Study. Int J Cardiol 215: 325–331 Doi https://doi.org/10.1016/j.ijcard.2016.04.129
11. Hernandez-Vela A, Gatta C, Escalera S, Igual L, Martin-Yuste V, Sabate M, Radeva P (2012) Accurate coronary centerline extraction, caliber estimation, and catheter detection in angiographies. IEEE Trans Inf Technol Biomed 16:1332–1340. https://doi.org/10.1109/titb.2012.2220781
12. Kang D, Slomka PJ, Nakazato R, Arsanjani R, Cheng VY, Min JK, Li D, Berman DS, Kuo CCJ, Dey D (2013) Automated knowledge-based detection of nonobstructive and obstructive arterial lesions from coronary CT angiography. Medical Physics 40:40. https://doi.org/10.1118/1.4794480
13. Kelm BM, Mittal S, Zheng Y, Tsymbal A, Bernhardt D, Vega-Higuera F, Zhou SK, Meer P, Comaniciu D (2011) Detection, grading and classification of coronary stenoses in computed tomography angiography.In: Fichtinger G., Martel A., Peters T. (eds) Medical Image Computing and Computer-Assisted Intervention – MICCAI 2011. Lect Notes Comput Sc, 6893: 25-32.
14. Kirisli HA, Schaap M, Metz CT, Dharampal AS, Meijboom WB, Papadopoulou SL, Dedic A, Nieman K, de Graaf MA, Meijs MFLet al (2013) Standardized evaluation framework for evaluating coronary artery stenosis detection, stenosis quantification and lumen segmentation algorithms in computed tomography angiography. Med Image Anal 17: 859–876 Doi https://doi.org/10.1016/j.media.2013.05.007
15. Lee W, Choi GJ, Cho SW (2017) Numerical study to indicate the vulnerability of plaques using an idealized 2D plaque model based on plaque classification in the human coronary artery. Med Biol Eng Comput 55:1379–1387. https://doi.org/10.1007/s11517-016-1602-x
16. Li C, Xu C, Gui C, Fox MD (2010) Distance regularized level set evolution and its application to image segmentation. IEEE Trans Image Process 19:3243–3254. https://doi.org/10.1109/tip.2010.2069690
17. Mahapatra D (2017) Semi-supervised learning and graph cuts for consensus based medical image segmentation. Pattern Recogn 63: 700–709. https://doi.org/10.1016/j.patcog.2016.09.030
18. Mahapatra D, Schuffler PJ, Tielbeek JAW, Makanyanga JC, Stoker J, Taylor SA, Vos FM, Buhmann JM (2013) Automatic detection and segmentation of Crohn's disease tissues from abdominal MRI. IEEE Trans Med Imaging 32:2332–2347. https://doi.org/10.1109/tmi.2013.2282124
19. Renard F, Yongyi Y (2008) Image analysis for detection of coronary artery soft plaques in MDCT images. 5th IEEE International Symposium on Biomedical Imaging: From Nano to Macro, City, pp 25-28
20. Rinck D, Krüger S, Reimann A, Scheuering M (2006) Shape-based segmentation and visualization techniques for evaluation of atherosclerotic plaques in coronary artery disease. SPIE, City, pp 61410G
21. Roger VL, Go AS, Lloyd-Jones DM, Benjamin EJ, Berry JD, Borden WB, Bravata DM, Dai S, Ford ES, Fox CSet al (2012) Heart disease and stroke statistics—2012 update a report from the American Heart Association. Circulation 125: E2-E220 Doi https://doi.org/10.1161/CIR.0b013e31823ac046
22. Rubin GD, Leipsic J, Schoepf UJ, Fleischmann D, Napel S (2014) CT angiography after 20 years: a transformation in cardiovascular disease characterization continues to advance. Radiology 271:633–652. https://doi.org/10.1148/radiol.14132232
23. Takaoka H, Funabashi N, Ozawa K, Kobayashi Y (2013) Co-existing multiple vulnerable plaque characteristic factors in single non-obstructive non calcified or mixed plaques in coronary arteries on CT could predict occurrence of major cardiac events on follow-up for a median of 103 months. Circulation 128:11225
24. Takaoka H, Funabashi N, Uehara M, Ozawa K, Kobayashi Y (2013) Number of vulnerable plaque characteristics that are required in a single non-calcified plaque on CT to be at high risk of causing major adverse cardiovascular events. J Am Coll Cardiol 61: E1157. https://doi.org/10.1016/s0735-1097(13)61157-2
25. Tessmann M, Vega-Higuera F, Fritz D, Scheuering M, Greiner G (2009) Multi-scale feature extraction for learning-based classification of coronary artery stenosis. SPIE, City, pp 726002
26. Toumoulin C, Boldak C, Garreau M, Boulmier D (2003) Coronary characterization in multi-slice computed tomography. Computers in Cardiology, City, pp 749–752
27. Valencia MAZ (2011) Methods for automation of vascular lesions detection in computed tomography images. Universidad de los Andes, City
28. Wang Y, Liatsis P (2009) A fully automated framework for segmentation and stenosis quantification of coronary arteries in 3D CTA imaging. 2009 Second International Conference on Developments in eSystems Engineering, City, pp 136-140
29. Wesarg S, Khan MF, Firle EA (2006) Localizing calcifications in cardiac CT data sets using a new vessel segmentation approach. J Digit Imaging 19:249–257. https://doi.org/10.1007/s10278-006-9947-6
30. Yang G, Kitslaar P, Frenay M, Broersen A, Boogers MJ, Bax JJ, Reiber JHC, Dijkstra J (2012) Automatic centerline extraction of coronary arteries in coronary computed tomographic angiography. Int J Cardiovasc Imaging 28:921–933. https://doi.org/10.1007/s10554-011-9894-2
31. Zhang J, Zhao H, Liang J (2013) Continuous rotation invariant local descriptors for texton dictionary-based texture classification. Comput Vis Image Underst 117:56–75. https://doi.org/10.1016/j.cviu.2012.10.004
32. Zhao F, Liang J, Chen X, Liu J, Chen D, Yang X, Tian J (2016) Quantitative analysis of vascular parameters for micro-CT imaging of vascular networks with multi-resolution. Med Biol Eng Comput 54:511–524. https://doi.org/10.1007/s11517-015-1337-0
33. Zhao F, Liu J, Qu X, Xu X, Chen X, Yang X, Cao F, Liang J, Tian J (2014) In vivo quantitative evaluation of vascular parameters for angiogenesis based on sparse principal component analysis and aggregated boosted trees. Phys Med Biol 59:7777–7791. https://doi.org/10.1088/0031-9155/59/24/7777
34. Zuluaga MA, Magnin IE, Hernandez Hoyos M, Delgado Leyton EJF, Lozano F, Orkisz M (2011) Automatic detection of abnormal vascular cross-sections based on density level detection and support vector machines. Int J Comput Assist Radiol Surg 6:163–174. https://doi.org/10.1007/s11548-010-0494-8

Fengjun Zhao received the Ph.D degree in Signal and Information Processing from Xidian University in 2015. He is now a lecturer in Northwest University, focusing on medical image processing.

Bin Wu received the BEng degree in Internet of Things Engineering from Northwest University. She is now pursuing a Master's degree in Computer Application Technology from Northwest University.

Fei Chen received the BEng degree in Biomedical Engineering from Xidian University. She is now a Ph.D candidate in Pattern Recognition and Intelligence Systems from Xidian University.

Xin Cao received the Ph.D degree from Xidian University in 2016. He is now a lecturer in Northwest University and devoted to the preclinical research of Cerenkov imaging and its applications.

Huangjian Yi received the Ph.D degree from Xidian University in 2013. She is now a lecturer from Northwest University, whose research interests are the algorithms for fluorescent molecular imaging.

Yuqing Hou received the MEng degrees from Northwest University and Doshisha University, respectively. She is now a professor from Northwest University and has directed many research projects.

Xiaowei He received the Ph.D degree from Xidian University in 2011. He is now a professor and deputy dean of the graduate school in Northwest University, focusing on multi-modality molecular imaging.

Jimin Liang received the Ph.D degree from Xidian University in 2000. He is now a professor in Xidian University, who is skilled in medical imaging and has published more than 50 journal papers.